

# Raman spectroscopy on cubic and hexagonal $\text{SrMnO}_3$

A. Sacchetti\*, M. Baldini, P. Postorino

INFM and Dipartimento di Fisica, Università “La Sapienza”, P.le A. Moro 4, I-00187 Roma, Italy.

C. Martin, A. Maignan

Laboratoire CRISMAT-UMR, 6508 ENSI CAEN, 6, Marechal Juin, 14050 Caen, France.

We report on the first optical characterization of both cubic and hexagonal  $\text{SrMnO}_3$ . Room-temperature Raman spectra collected by means of a micro-Raman spectrometer are shown. The spectrum of the cubic compound is characterized by weak and broad bands in agreement with group-theory which predicts no Raman-active phonons for this compound. On the other hand, the spectrum of the hexagonal compound shows six narrow peaks ascribed to one-phonon processes. A complete polarization analysis of the spectra collected from a single crystallite allows us to completely assign the symmetries of the six observed peaks. Atomic displacements for each phonon peaks are also proposed.

## I. INTRODUCTION

In the last years, a remarkable experimental and theoretical effort was devoted to the study of colossal magneto-resistance manganites  $A_{1-x}A'_x\text{MnO}_3$  ( $A$  is a trivalent rare-earth and  $A'$  is a divalent alkaline earth). The peculiar properties of these systems have attracted much attention owing to their possible technological applications in the field of magnetic devices and, on the side of basic physics, to the possibility of disentangling the delicate interplay among the different microscopic interactions which govern their often uncommon behavior [1, 2]. The  $T - x$  (temperature-doping) phase diagram of manganites is typically very rich and presents a large number of structural, magnetic, and conducting phases [3]. Experimental and theoretical studies on doped compounds ( $0 < x < 1$ ) have contributed to build up a rather general framework, where a key role is played by the oxygen-mediated magnetic interactions among the Mn ions and the electron-phonon coupling triggered by a Jahn-Teller distortion of the  $\text{MnO}_6$  octahedra. In particular, the strength of the charge-lattice coupling is directly related to the average Mn valence state (i.e. to  $x$ ) and to the spatial arrangements of the  $\text{MnO}_6$  sub-lattice. Much less attention was devoted to the  $x = 1$  end compounds and there are very few studies, mainly appeared in early papers, reporting on  $\text{SrMnO}_3$  (SMO), despite its importance. SMO is indeed the parent compound of one of the most studied manganite family ( $\text{La}_{1-x}\text{Sr}_x\text{MnO}_3$ ) and of electron doped manganites series such as  $\text{Sr}_{1-x}\text{Ce}_x\text{MnO}_3$ , which are nowadays of utmost interest. Moreover, the possibility of switching the lattice symmetry of SMO from cubic to hexagonal depending on the growing parameters could give unique opportunities of studying the role of the spatial arrangements of the  $\text{MnO}_6$  network. Since optical spectroscopies

have been largely and successfully employed to study manganites [4], in the present paper we report the first Raman characterization of cubic (cSMO) and hexagonal (hSMO)  $\text{SrMnO}_3$  and a complete assignment of the observed Raman active modes.

## II. EXPERIMENTAL

The SMO polycrystalline samples were synthesized with standard solid-state reaction from stoichiometric mixtures of  $\text{SrCO}_3$  and  $\text{MnO}_2$  at  $1500^\circ\text{C}$  [5, 6]. The sample synthesized in air is characterized by an hexagonal structure. The oxygen-deficient cubic compound was obtained in Ar-flow. Then, the cubic compound was annealed for 24 h at  $600^\circ\text{C}$ , in a 100 bar  $\text{O}_2$  atmosphere in order to reach the  $\text{O}_3$  stoichiometry. A detailed characterization of both sample was performed by means of X-ray diffraction and magnetization measurements. The hexagonal and cubic compounds belong to the  $P6_3/mmc$  and  $Pm3m$  space groups respectively, both samples showing a low-temperature antiferromagnetic phase with a Neél temperature of 278 K (hexagonal) and 260 K (cubic) [7, 8].

Raman-scattering measurements were performed in the backscattering geometry using a confocal Raman microspectrometer (Labram Infinity, Jobin Yvon). The spectrometer was equipped with an He-Ne laser source (we used the 632.81 nm line with a power of about 15 mW on the sample surface) and a cooled charge coupled device (CCD) detector to collect the scattered light dispersed by a 1800 lines/mm grating. The notch filter, used to reject the elastically scattered light, does not allow reliable measurements below  $200 \text{ cm}^{-1}$ . The microscope equipped with a  $20\times$  objective enables for a spatial resolution gain of a few microns on the sample surface. Room temperature Raman spectra of SMO (hexagonal and cubic), with a resolution of about  $3 \text{ cm}^{-1}$ , were collected over the  $200$ - $1100 \text{ cm}^{-1}$  spectral range.

Sample's homogeneity was checked by comparing the spectra collected by focusing the laser beam on differ-

\*corresponding author. Email: sacchetti@phys.ethz.ch, Tel.: +41 44 6332241, Fax: +41 44 6331072

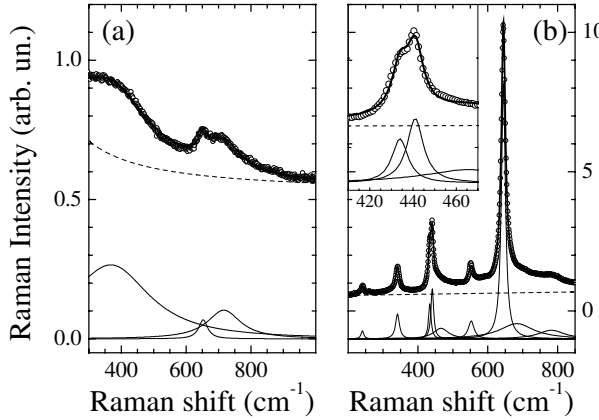


FIG. 1: Raman spectrum of cubic (a) and hexagonal (b) SMO (open circles). Best-fit curves (thick solid lines), fitting components (thin solid lines), and background contributions (dashed lines) are also shown for both compounds. Fitting components in (b) have been downshifted for sake of clarity. Note the different vertical scale in (a) and (b). In (b) the inset shows the presence of a double one-phonon peak at around  $440\text{ cm}^{-1}$ .

ent spots of the samples surface. The Raman spectra of cSMO have shown a quite good reproducibility whereas remarkable fluctuations of the band intensities were observed from point to point in the hSMO. Bearing in mind that the incident beam has a definite linear polarization, the presence of crystallites randomly oriented on the micron scale can account for the observed fluctuations. Optical and spectroscopic analysis of very small fragments of our hSMO sample confirmed this hypothesis and allowed us to select some small single crystals to be analyzed. A polarization analysis of the Raman signal was thus carried out on a very small single crystal of the hSMO (about  $100 \times 20\text{ }\mu\text{m}^2$ ) using a rotating platform with fine tilting movements to carefully align the sample surface and a polarization analyzer placed just in front of the monochromator entrance slit.

### III. RESULTS AND DISCUSSION

The typical Raman spectrum of the cSMO and a representative Raman spectra of the hSMO are shown in Fig. 1(a) and (b) respectively. Bearing in mind that the intensities of the two spectra are normalized to the same acquisition time, it is well evident that the Raman signal of the cSMO sample is much less structured and, on average, much smaller (roughly one order of magnitude) than that of the hSMO (note the different vertical scales in panels (a) and (b) of Fig. 1). This finding is consistent with group-theory which predicts 8 Raman active phonons for the hexagonal symmetry ( $P6_3/mmc$  space group) and none for the cubic perovskite structure. The weak signal collected for the cubic sample is thus to be ascribed to Raman-forbidden modes possibly activated

by lattice disorder or second-order Raman scattering. In the case of the hSMO compound, which shows several well defined peaks in the Raman spectrum (notice the two peaks structure in the inset of Fig. 1(b)), the total irreducible representation of the Raman-active phonons can be determined starting from the point-group symmetry, that is [9]:

$$\Gamma_{\text{Ram}} = 2A_{1g} + 2E_{1g} + 4E_{2g} \quad (1)$$

The high signal to noise ratio of the data allows for a careful lineshape analysis. Both spectra were fitted by means of a linear combination of damped harmonic oscillators (DHO) and a background term [10, 11]:

$$I(\nu) = I_{\text{BKG}}(\nu) + \sum_{i=1}^N \frac{A_i \Gamma_i^2 \nu_i \nu}{(\nu^2 - \nu_i^2)^2 + \Gamma_i^2 \nu^2} \quad (2)$$

where  $I_{\text{BKG}}(\nu)$  is the background contribution and the second term is the contribution from  $N$  phonon peaks of frequency  $\nu_i$ , width  $\Gamma_i$ , and amplitude  $A_i$ . We used  $N = 12$  phonon peaks plus a linear  $I_{\text{BKG}}(\nu)$  for the cSMO and  $N = 3$  phonon peaks plus a diffusive electronic  $I_{\text{BKG}}(\nu)$  [10, 11] for the cubic compound. The best-fit curves and single fitting-components are also shown in Fig. 1, whereas the corresponding best-fit phonon frequencies  $\nu_i$  and widths  $\Gamma_i$ , are reported in tab. I.

Before focusing on the analysis of the hexagonal compound it is worth to notice that it has been necessary to introduce the diffusive term (see the dashed line in Fig. 1(a)) due to the scattering of charge carriers, only for the cubic sample which shows a higher conductivity than that of the hexagonal compound [12].

Looking at the best-fit parameters reported in tab. I for the hexagonal sample we notice six rather narrow peaks

| Cubic                        |                                 |
|------------------------------|---------------------------------|
| $\nu_i$ ( $\text{cm}^{-1}$ ) | $\Gamma_i$ ( $\text{cm}^{-1}$ ) |
| 405                          | 296                             |
| 652                          | 33                              |
| 719                          | 125                             |

| Hexagonal                    |                                 |           |                |
|------------------------------|---------------------------------|-----------|----------------|
| $\nu_i$ ( $\text{cm}^{-1}$ ) | $\Gamma_i$ ( $\text{cm}^{-1}$ ) | 1-ph/m-ph | Label          |
| 243                          | 9                               | 1-ph      | P <sub>1</sub> |
| 344                          | 13                              | 1-ph      | P <sub>2</sub> |
| 434                          | 9                               | 1-ph      | P <sub>3</sub> |
| 441                          | 9                               | 1-ph      | P <sub>4</sub> |
| 467                          | 52                              | m-ph      |                |
| 552                          | 20                              | 1-ph      | P <sub>5</sub> |
| 644                          | 14                              | 1-ph      | P <sub>6</sub> |
| 686                          | 119                             | m-ph      |                |
| 783                          | 89                              | m-ph      |                |

TABLE I: Phonon frequencies  $\nu_i$  and widths  $\Gamma_i$  for cSMO (top table) and for hSMO (bottom table). For hSMO 1-phonon (1-ph) or multi-phonon (m-ph) contributions are also indicated.

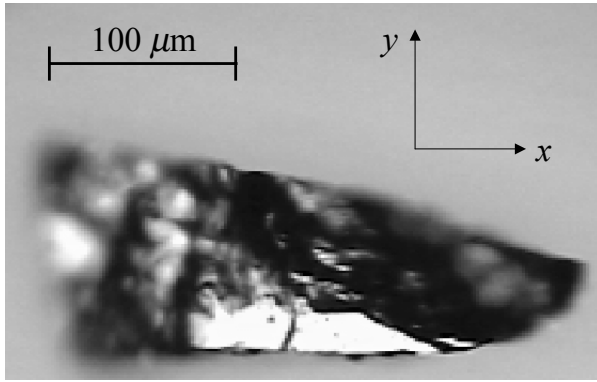


FIG. 2: Picture (taken with the microscope of the micro-Raman apparatus) of the crystallite employed for polarization dependent measurements.

( $\Gamma_i \leq 20 \text{ cm}^{-1}$ ), labelled P<sub>1</sub>-P<sub>6</sub> in increasing-frequency order, and three broad peaks ( $\Gamma_i > 50 \text{ cm}^{-1}$ ). Since no broadening factors are reasonably expected for the hSMO, we tentatively ascribe the six P<sub>1</sub>-P<sub>6</sub> peaks to one-phonon processes out of the 8 predicted, and the other ones to multi-phonon processes. This assignment is confirmed and detailed by the polarization analysis we are going to discuss. By scratching the polycrystalline sample we were able to obtain several crystallites. One of them, characterized by a flat surface (see Fig. 2) which simple test measurements suggested to be an  $a - c$  plane, was chosen for the polarization analysis. The flat surface of the crystallite was roughly aligned perpendicular to the laser beam using the image from the microscope. In order to carefully determine the orientation of the crystallite, a preliminary set of measurements was performed, rotating the crystallite from 0° to 200° with a 5° step. A configuration with scattered polarization parallel to the incident one was selected. The angle dependence of the spectrum is shown in Fig. 3. It can be noted that the P<sub>2</sub> (344 cm<sup>-1</sup>) and P<sub>3</sub> (434 cm<sup>-1</sup>) peaks show the same dependence and periodicity and thus the same symmetry, whereas the P<sub>6</sub> (644 cm<sup>-1</sup>) peak is characterized by a clearly different behavior. The intensities (integrated areas) of the P<sub>2</sub>, P<sub>3</sub>, and P<sub>6</sub> peaks were determined at each angle by means of a single-peak fitting procedure. The resulting angle-dependencies of the intensities of the three peaks were then analyzed by means of three model functions based on group-theory and determined as follows. We exploited the forms of the Raman tensors for each allowed phonon symmetry [9]:

$$A_{1g} : \begin{pmatrix} A & 0 & 0 \\ 0 & A & 0 \\ 0 & 0 & B \end{pmatrix} \quad E_{1g} : \begin{pmatrix} 0 & 0 & 0 \\ 0 & 0 & C \\ 0 & C & 0 \end{pmatrix}, \begin{pmatrix} 0 & 0 & C \\ 0 & 0 & 0 \\ C & 0 & 0 \end{pmatrix}$$

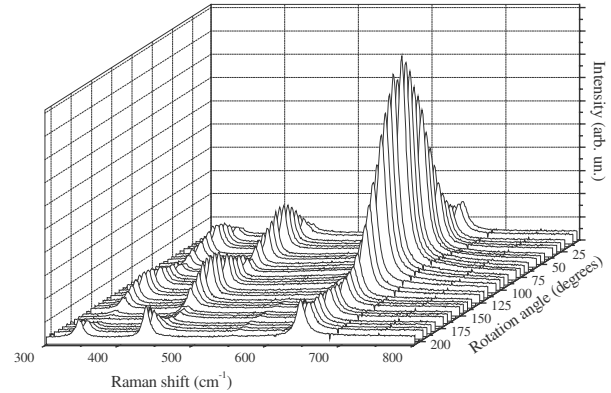


FIG. 3: Rotation-angle dependence of the Raman spectrum of the crystallite shown in Fig. 2. The origin of the angle scale is arbitrary.

$$E_{2g} : \begin{pmatrix} -D & 0 & 0 \\ 0 & D & 0 \\ 0 & 0 & 0 \end{pmatrix}, \begin{pmatrix} 0 & D & 0 \\ D & 0 & 0 \\ 0 & 0 & 0 \end{pmatrix} \quad (3)$$

and the well-known relation for the Raman intensity:

$$I = |\hat{\varepsilon} \alpha \hat{\varepsilon}'|^2 \quad (4)$$

where  $\hat{\varepsilon}$  and  $\hat{\varepsilon}'$  are the polarization of the incident and the scattered light respectively and  $\alpha$  is the Raman tensor. Assuming an arbitrary tilting angle  $\beta$  between the laser beam and the crystal  $c$ -axis, for each symmetry an analytical model function for the angle-dependence of the intensity was determined. Since the orientation of the crystal is unknown *a priori* we have also introduced an offset angle  $\theta_0$  for the measured rotation angle  $\theta$  so that  $\theta - \theta_0$  is the angle between the incident polarization  $\hat{\varepsilon}$  and the crystal  $a$ -axis. The analytical expressions of the so-obtained model functions are simple although long and they are not reported here.

Exploiting the calculated model functions, a fitting procedure was applied to the angle dependence of the intensities of P<sub>2</sub>, P<sub>3</sub>, and P<sub>6</sub> peaks, assuming  $\beta$ ,  $\theta_0$ , and the components of the considered Raman tensor assigned to each peak as free fitting-parameters. Good quality fits were obtained only assigning the E<sub>1g</sub> symmetry to the P<sub>2</sub> and P<sub>3</sub> peaks and the A<sub>1g</sub> symmetry to the P<sub>6</sub> peak with a best fit value of 72° for  $\beta$ . This result confirms that the flat surface of the crystallite is an  $a - c$  plane and that  $\hat{\varepsilon}$  does not lie in this plane but forms a small angle (18°) with it. The  $\theta_0$  best fit value allowed us to conclude that the  $c$  axis is parallel to the  $y$  axis in Fig. 2.

Exploiting the orientation of the crystallite thus determined and monitoring the Raman signal, we were able to carefully align the flat  $a - c$  surface of the crystallite, orthogonally to the laser beam. In this case  $\beta = 90^\circ$  and  $\theta_0$  can be set to 0° so that the expressions for the

angle-dependence of the intensities of the phonon peaks are strongly simplified. Thus in the parallel polarization geometry ( $\hat{\varepsilon} = (\cos \theta, 0, \sin \theta) = \hat{\varepsilon}'$  in the base of crystal axes) one has:

$$I_{A_{1g}}^{\parallel} = (A - B)^2 \cos^4 \theta + 2B(A - B) \cos^2 \theta + B^2 \quad (5)$$

$$I_{E_{1g}}^{\parallel} = 4C^2 \sin^2 \theta \cos^2 \theta$$

$$I_{E_{2g}}^{\parallel} = D^2 \cos^4 \theta$$

and in the orthogonal polarization geometry ( $\hat{\varepsilon} = (\cos \theta, 0, \sin \theta)$  and  $\hat{\varepsilon}'(-\sin \theta, 0, \cos \theta)$ ) one has:

$$I_{A_{1g}}^{\perp} = (A - B)^2 \sin^2 \theta \cos^2 \theta \quad (6)$$

$$I_{E_{1g}}^{\perp} = C^2 - 4C^2 \sin^2 \theta \cos^2 \theta$$

$$I_{E_{2g}}^{\perp} = D^2 \sin^2 \theta \cos^2 \theta$$

with  $A$ ,  $B$ ,  $C$  and  $D$  elements of the Raman tensors (see eq. 3). We choose to analyze two high-symmetry configurations, namely:  $\theta = 0^\circ$  ( $\hat{\varepsilon}$  parallel to the  $a$ -axis) and  $\theta = 90^\circ$  ( $\hat{\varepsilon}$  parallel to the  $c$ -axis). The intensities for the three symmetries  $A_{1g}$ ,  $E_{2g}$  and  $E_{1g}$  can be calculated in these high symmetry configurations exploiting eqs. 5 and 6, and the results are reported in tab. II. Long acquisition-time spectra were then collected for the selected configurations in order to obtain a complete assignment of the observed phonon modes. Measurements, shown in Fig. 4, were performed in both parallel and orthogonal polarization. Comparing the data in Fig. 4 with tab. II the assignment of the  $P_2$ ,  $P_3$ , and  $P_6$  peaks obtained from the preliminary measurements is confirmed. Indeed, either for  $\theta = 0^\circ$  or  $90^\circ$ ,  $P_2$  and  $P_3$  peaks are both visible in orthogonal polarization and vanish in parallel polarization as expected for the  $E_{1g}$  symmetry, whereas  $P_6$  peak is apparent in the parallel polarization and vanishes in the orthogonal polarization, as expected for the  $A_{1g}$  symmetry. Four  $E_{2g}$  modes and one  $A_{1g}$  mode remain to be assigned (see eq. 1). The  $P_4$  peak is clearly visible in parallel polarization at  $\theta = 0^\circ$  and its intensity drops to zero at  $\theta = 90^\circ$ , whereas in orthogonal polarization it vanishes at both angles. Comparing this behavior

|                         | $\theta = 0^\circ$ | $\theta = 90^\circ$ |
|-------------------------|--------------------|---------------------|
| $I(A_{1g})^{\parallel}$ | $A^2$              | $B^2$               |
| $I(A_{1g})^{\perp}$     | 0                  | 0                   |
| $I(E_{1g})^{\parallel}$ | 0                  | 0                   |
| $I(E_{1g})^{\perp}$     | $C^2$              | $C^2$               |
| $I(E_{2g})^{\parallel}$ | $D^2$              | 0                   |
| $I(E_{2g})^{\perp}$     | 0                  | 0                   |

TABLE II: Calculated intensities of the three phonon symmetries in both parallel ( $\parallel$ ) and orthogonal ( $\perp$ ) configurations at high-symmetry angles. The constants  $A$ ,  $B$ ,  $C$ , and  $D$  are the components of the Raman tensors (see eq. 3).

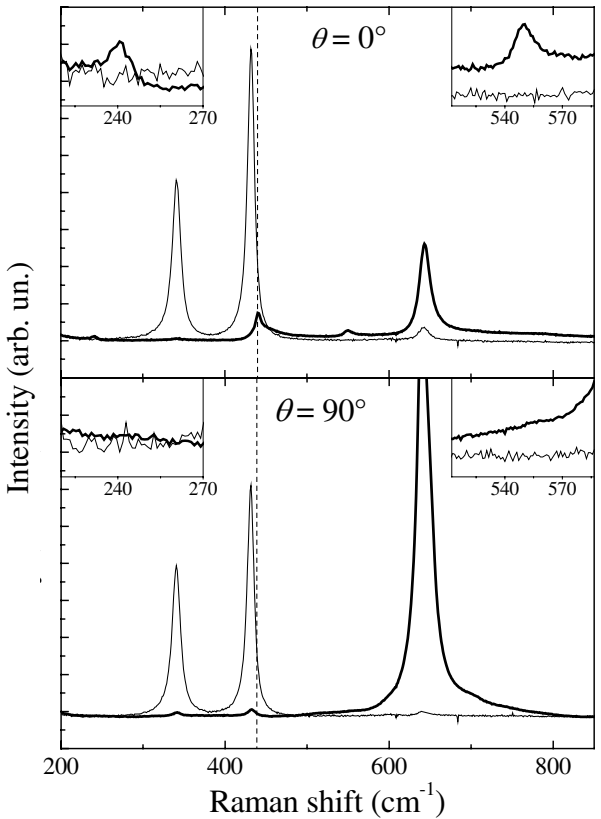


FIG. 4: Raman spectra of hSMO at  $\theta = 0^\circ$  (top panel) and  $\theta = 90^\circ$  (bottom panel) in both parallel (thick lines) and orthogonal (thin lines) configurations. Vertical dashed lines mark the position of  $P_4$  peak. Insets show magnifications in the regions of  $P_1$  and  $P_5$  peaks.

with tab. II we can assign the  $P_4$  peak to the  $E_{2g}$  symmetry. The behavior of peaks  $P_1$  and  $P_5$  is analogous (see the insets in Fig. 4) to that of the  $P_4$  phonon and opposite to the  $P_6$  peak. Therefore  $P_1$  and  $P_5$  modes are also ascribed to the  $E_{2g}$  symmetry. Thus the symmetry of all the six observed phonon peaks was determined as reported in tab. III.

From the point-group symmetry of the crystal, the symmetry-reduced coordinates for each phonon-symmetry can be determined (see Fig. 5) [9]. Owing to the quite large difference between the atomic masses of

| Label | $\nu_i$ (cm $^{-1}$ ) | Assignment  | Atom |
|-------|-----------------------|-------------|------|
| P1    | 243                   | $E_{2g}(2)$ | Mn   |
| P2    | 344                   | $E_{1g}(1)$ | Mn   |
| P3    | 434                   | $E_{1g}(2)$ | O    |
| P4    | 441                   | $E_{2g}(3)$ | O    |
| P5    | 551                   | $E_{2g}(4)$ | O    |
| P6    | 644                   | $A_{1g}(2)$ | O    |

TABLE III: Assignment of the 1-phonon peaks observed in hSMO.

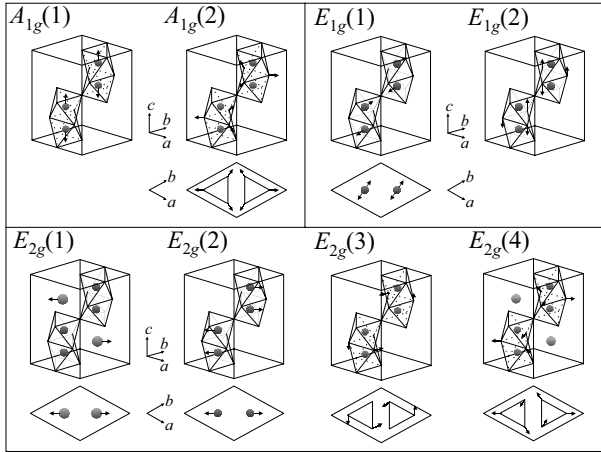


FIG. 5: Symmetry reduced atomic-displacements for Raman active phonon modes in hSMO. Sr (Mn) atoms are indicated by large (small) circles.

Sr, Mn, and O, it is reasonable to assume that the observed phonons are almost pure modes, i.e. they mainly involve displacements of a single atomic species. Therefore it is possible to assign the phonon peaks appearing in the spectra to the atomic displacements shown in Fig. 5. As a rule of thumb we can assume that phonons involving displacements of lighter ions have larger frequencies and moreover it is generally correct to assume that stretching modes have frequencies higher than bending modes. On the basis of these assumptions, we ascribe peaks  $P_2$  and  $P_3$  to the  $E_{1g}(1)$  (Mn displacements) and  $E_{1g}(2)$  (O displacements) modes respectively according with the notation used in Fig. 5. As to the  $P_6$  peak ( $A_{1g}$  symmetry) its high vibrational frequency suggests the assignment of this phonon to the  $A_{1g}(2)$  mode (O displacements) rather than  $A_{1g}(1)$  mode (Mn displacements). This assignment is consistent with that reported for isostructural  $\text{BaRuO}_3$  [13]. The remaining peaks  $P_1$ ,  $P_4$ , and  $P_5$  have  $E_{2g}$  symmetry. Bearing in mind that in  $\text{BaRuO}_3$  the  $E_{2g}(1)$  mode involving Ba-displacements is centered

at  $90 \text{ cm}^{-1}$  (Ref.[13]) and that the ratio between atomic masses of Ba and Sr is 1.57, we expect the  $E_{2g}(1)$  phonon in hSMO to have a frequency well below our experimental lower frequency-limit of  $200 \text{ cm}^{-1}$ . Therefore, exploiting the aforementioned assumptions, we ascribe  $P_1$  peak to the  $E_{2g}(2)$  mode (Mn displacement), whereas the  $P_4$  peak is assigned to the  $E_{2g}(3)$  mode (O bending), and the  $P_5$  peak is ascribed to the  $E_{2g}(4)$  mode (O stretching).

The assignment of the six one-phonon peaks observed in hSMO is summarized in tab. III.

#### IV. CONCLUSIONS

In summary, we reported the first optical characterization of both the cubic and hexagonal  $\text{SrMnO}_3$  manganite, performed by means of Raman spectroscopy. Consistently with group-theory, which does not predict Raman-active peaks in the cubic compound, the spectrum of this compound substantially consists of very weak and broad structures, probably due to Raman-forbidden modes and/or multi-phonon processes. On the other hand, the spectrum of the hexagonal compound shows six sharp peaks ascribed to one-phonon processes. Exploiting our micro-Raman apparatus, a polarization analysis was performed on a small crystallite of the hexagonal sample. A preliminary set of measurements allowed us to assign the symmetry of the main phonon peaks and to carefully determine the orientation of the crystallite. A second set of measurements was performed, aligning the crystallite with the  $a - c$  plane orthogonal to the optical axis. By using these data, a complete assignment of all the observed Raman-active phonon peaks was performed. This study by micro Raman on small manganite crystallite show that a good accuracy can be achieved for these transition metal oxides. It opens thus the route to the study of other compounds such as  $\text{YMnO}_3$  for instance in which the trivalent manganese adopts a five fold coordination in  $\text{MnO}_5$  trigonal bipyramids.

---

[1] Millis AJ. *Nature*. 1998; **392**: 147.

[2] Fontcuberta J. *Phys. World*. 1999; **Feb**: 33.

[3] Dagotto E, Hotta T, Moreo A. *Phys. Rep.* 2001; **344**: 1.

[4] Postorino P, Congeduti A, Degiorgi E, Itié JP, Munsch P. *Phys. Rev. B*. 2002; **65**: 224102. Dediu V, Ferdegini C, Matacotta FC, Nozar P, Ruani G. *Phys. Rev. Lett.* 2000; **84**: 4489. Iliev MN, Abrashev MV, Lee HG, Popov VN, Sun YY, Thomsen C, Meng RL, Chu CW. *Phys. Rev. B*. 1998; **57**: 2872.

[5] Hervieu M, Martin C, Maignan A, Van Tendeloo G, Jirak Z, Hejtmanek J, Barnabé A, Thopart D, Raveau B. *Chem. Mater.* 2000; **12**: 1456.

[6] Chmaissem O, Dabrowski B, Kolesnik S, Mais J, Brown DE, Kruk R, Prior P, Pyles B, Jorgensen JD. *Phys Rev B*. 2001; **64**: 134412.

[7] Battle PD, Gibb TC, Jones CW. *J. Solid State Chem*. 1998; **74**: 60.

[8] Takeda T, Ohara S. *J. Phys. Soc. Jpn.* 1974; **37**: 275.

[9] Fateley WG, Dollish FR, McDevitt HT, Bentley FF. *Infrared and Raman Selection Rules for Molecular and Lattice Vibrations: The Correlation Method*; Wiley-Interscience: New York, USA, 1972.

[10] Yoon S, Liu HL, Schollerer G, Cooper SL, Han PD, Payne DA, Cheong SW, Fisk Z. *Phys. Rev. B*. 1998; **58**: 2795.

[11] Congeduti A, Postorino P, Caramagno E, Nardone M, Kumar A, Sarma DD. *Phys. Rev. Lett.*; 2001; **86**: 1251.

[12] Hashimoto S, Iwahara H. *J. Electroceram*. 2000; **1**: 225.

[13] Lee YS, Noh TW, Park JH, Lee KB, Cao G, Crow JE, Lee MK, Eom CB, Oh EJ, In-Sang Yang. *Phys. Rev. B* 2002; **65**: 235113.